Photoionization of Fe^{7+} from the ground and metastable states

S. S. Tayal*
Department of Physics, Clark Atlanta University, Atlanta, Georgia 30314, USA

O. Zatsarinny†
Department of Physics and Astronomy, Drake University, Des Moines, Iowa 50311, USA

(Received 1 October 2014; published 26 January 2015)

The B-spline Breit-Pauli R-matrix method is used to investigate the photoionization of Fe^{7+} from the ground and metastable states in the energy region from ionization thresholds to 172 eV. The present calculations were designed to resolve the large discrepancies between recent measurements and available theoretical results. The multiconfiguration Hartree-Fock method in connection with B-spline expansions is employed for an accurate representation of the initial- and final-state wave functions. The close-coupling expansion includes 99 fine-structure levels of the residual Fe^{8+} ion in the energy region up to $3s^23p^54s$ states. It includes levels of the $3s^23p^6$, $3s^23p^53d$, $3s^23p^54s$, and $3s3p^63d$ configurations and some levels of the $3s^23p^43d^2$ configuration which lie in the energy region under investigation. The present photoionization cross sections in the length and velocity formulations exhibit excellent agreement. The present photoionization cross sections agree well with the Breit-Pauli R-matrix calculation by Sossah *et al.* and the TOPbase data in the magnitude of the background nonresonant cross sections but show somewhat richer resonance structures, which qualitatively agree with the measurements. The calculated cross sections, however, are several times lower than the measured cross sections, depending upon the photon energy. The cross sections for photoionization of metastable states were found to have approximately the same magnitude as the cross sections for photoionization of the ground state, thereby the presence of metastable states in the ion beam may not be the reason for the enhancement of the measured cross sections.

DOI: 10.1103/PhysRevA.91.013413 PACS number(s): 32.80.Zb, 32.80.Fb

I. INTRODUCTION

Photoionization of atoms and ions is one of the main elementary processes of the electromagnetic radiation interaction with matter, and the photoionization cross sections are of great significance in many applications such as plasma physics, the lighting industry, atmospheric science, and several fields of astrophysics. The photoionization of ions, especially ions of the transition metals Ti, Mn, Fe, and Ni, are also important in controlled thermonuclear fusion reactors. These metals appear as impurities from the fusion reactor walls, or they are deliberately released as diagnostic tracer elements. The photoionization processes of these ions directly affect cooling, transport, and confinement of plasma in different high-temperature fusion devices. Absolute cross sections for photoionization of these ions are also of great interest for model spectral emissions from stellar atmospheres, novas, and active galactic nuclei.

Despite the long history of their calculations and measurements, the photoionization cross sections for many ions remain uncertain. In high-temperature plasma environments atoms can be found in different ionic states. Therefore, plasma modeling requires studies of ionization and recombination processes along isonuclear sequences, i.e., for different ionic states of an element. Each ion has its specific atomic structure and there is significant change along the isonuclear sequences when various filled subshells are opened. This produces extreme difficulty in both theoretical studies of atomic structure and dynamical processes of these ions and the interpretation of experimental measurements. Another complication arises from the fact that many ions at high temperatures have a considerable population of metastable states. Usually, measurements cannot provide quantitative information on the metastable states in the ion beam and, thus, normally do not allow direct comparison with theoretical cross sections.

Iron is among the most astrophysically abundant elements, and hence its ions can serve as an important diagnostic tool in different astrophysical environments. For this reason, iron ions have received significant attention from both theory and experiment. Theoretically, photoionization of iron ions has been explored extensively as part of the Opacity Project [1] and Iron Project [2]. On the experimental side, photoionization measurements for iron ions were made using synchrotron radiation and an atomic-beam technique. The absolute single- and double-photoionization cross sections of singly charged Fe ions have been measured from 15.8 to 180 eV using the merged-beam technique [3]. Experimental and theoretical studies of the photoionization cross section of Fe^{4+} ion between 59 and 140 eV photon energy were reported by Bizau *et al.* [4]. The available R-matrix calculations describe qualitatively well the results of the experiment in the $3p \rightarrow 3d$ excitation region. Photoionization of Fe^{2+} through Fe^{6+} has been measured from their thresholds to 160 eV [5]. It was shown that the theoretical results tend to overestimate the intensity of the $3p \rightarrow 3d$ photoexcitations. In particular, an anomalously low value of the integrated oscillator strength is measured for the Fe^{2+} ion. Recently, cross sections for

*stayal@cau.edu
†oleg.zatsarinny@drake.edu

single photoionization of Fe^{3+}, Fe^{5+}, and Fe^{7+} ions have been measured at the high spectral resolutions of 0.04, 0.15, and 0.13 eV, respectively, by Gharaibeh *et al.* [6]. Absolute photoionization cross-section measurements were also performed using ion beams containing undetermined fractions of ions in their ground and metastable states. It makes their interpretation and comparisons with theory and other measurements difficult. Nevertheless, considerable differences from available theoretical results were noted.

Theoretical studies of structure and dynamical processes in transition metal atoms and ions with open $3d$ subshells are both challenging and interesting as discussed by Sossah *et al.* [7]. They investigated photoionization of K-like ions ($Z = 22$–26) using both nonrelativistic and Breit-Pauli R-matrix methods. They calculated photoionization cross sections from the ground $3s^2 3p^6 3d\ ^2D_{3/2}$ and metastable $3s^2 3p^6 3d\ ^2D_{5/2}$ states and found substantial changes in the photoionization spectra of K-like ions as $3p \rightarrow 3d$ excitation moves from the continuum to the bound part of the spectrum for $Z \geqslant 23$. The $3p \rightarrow 3d$ excitation energy for Fe^{7+} lies below the $3d$ ionization threshold and thus the photoionization spectrum of Fe^{7+} contains weaker and narrower Rydberg series of resonances with excitation of $3p$ electrons to autoionizing states with $n \geqslant 4$. As a result, the sum of oscillator strengths in the continuum decreases with increasing Z from $Z = 21$ to $Z = 26$. In the photoionization of Ca^+, Sc^{2+}, and Ti^{3+} the $3p \rightarrow 3d$ excitation energy is above the $3d$ threshold and giant resonances occur due to the $3s^2 3p^6 3d\ ^2D$–$3s^2 3p^5 3d^2\ ^2F^o$ transition, which decays through a Super-Coster-Kronig $3s^2 3p^5 3d^2$–$3s^2 3p^6 + e$ transition. The measurements by Gharaibeh *et al.* [6] were performed after the calculations by Sossah *et al.* [7], and no comparison of the measured results was made with the calculations of Sossah *et al.* [7]. The primary objective of our work is to present a comparison of various calculations with experiment and to investigate possible cause of discrepancies.

II. CALCULATIONS

A. Target wave functions

The final residual ionic states of Fe^{8+} in the present calculations were generated by combining the multiconfiguration Hartree-Fock (MCHF) and the B-spline box-based multichannel methods [8]. Specifically, the structure of the multichannel target expansions was chosen as

$$\Phi^J = \sum_{nl,LS} \{\phi(3s^2 3p^5) P(nl)\}^{LSJ} + \sum_{nl,LS} \{\phi(3s 3p^6) P(nl)\}^{LSJ} + a_{LSJ}\varphi(3s^2 3p^4 3d^2)^{LSJ} + b_{LSJ}\varphi(3s 3p^5 3d^2)^{LSJ}, \quad (1)$$

where $P(nl)$ denotes the wave function of the outer valence electron. The first two terms in the above expansion represent the entire $3s^2 3p^5 nl$ and $3s 3p^6 nl$ Rydberg series in Fe^{8+}, while the $3d^2$ states are represented by individual configuration-interaction (CI) expansions φ. They can be considered "perturbers" to the Rydberg series. The inner-core or short-range correlation is included through the CI expansion of the $\phi(3s^2 3p^5)$ and $\phi(3s 3p^6)$ ionic states. These expansions along with the perturber expansions φ were generated in separate multiconfiguration calculations using the program MCHF [9]. Multiconfiguration expansions φ include all single and double promotions from $3s$ and $3p$ orbitals to $3d$ and $4\bar{l}$ ($l = 0$–4) correlated orbitals, which are generated separately for each configuration. In order to keep the final expansions for the final Fe^{8+} states to a reasonable size, all contributions with expansion coefficients of magnitude less than 0.02 were neglected. Note that we also used separate CI expansions for the initial ground and metastable states that allowed us to include relaxation effects via state-specific one-electron orbitals.

The unknown functions $P(nl)$ for the outer valence electron were expanded in a B-spline basis, subject to the condition that the wave functions vanish at the boundary. The B-spline coefficients for the valence orbitals $P(nl)$, along with the coefficients $(a,b)_{LSJ}$ for the perturbers, were obtained by diagonalizing the atomic Breit-Pauli Hamiltonian, which includes all one-electron relativistic corrections. The above scheme yields a set of term-dependent one-electron orbitals for each valence orbital, also accounting for important interactions between the Rydberg series and the perturbers. Since such multichannel bound-state calculations generate different nonorthogonal sets of orbitals for each atomic state, their subsequent use in photoionization calculations is somewhat complicated. On the other hand, our configuration expansions for the atomic target states contained from 400 to 600 configurations for each state and hence could be used in the photoionization calculations with available computational resources.

Table I lists the Fe^{8+} target states included in the present photoionization calculations. The present calculated excitation energies are compared with the available experimental values from the NIST compilation [10] and other calculations. Storey *et al.* [11], Verma *et al.* [12], and Aggarwal *et al.* [13] reported energy levels and radiative rates for Fe^{8+} using well-tested computer codes. They considered different numbers of levels that were described by different CI expansions to account for electron correlation effects. Storey *et al.* [11] considered 140 levels of the $3s^2 3p^6$, $3s^2 3p^5 3d$, $3s^2 3p^5 4s$, $3s^2 3p^5 4p$, and $3s^2 3p^4 3d^2$ configurations in their SUPERSTRUCTURE [14] calculations, and Verma *et al.* [12] included 87 levels of the $3s^2 3p^6$, $3s^2 3p^5 3d$, $3s^2 3p^5 4l$ ($l = 0$–3), $3s 3p^6 3d$, $3s 3p^6 4s$, $3s 3p^6 4p$, and $3s^2 3p^5 5l$ ($l = 0$–2) configurations in the CIV3 structure calculation [15]. Aggarwal *et al.* [13] performed the most extensive calculations using the fully relativistic GRASP [16] and FAC [17] codes and carried out in-depth investigation of CI expansions by including various configurations of $n = 3$ and $n = 4$ complexes. They concluded that their GRASP results with 2471 levels are most accurate, with the accuracy of energies for many levels better than 1%. We have included these results for comparison in Table I. The lower part of the Fe^{8+} spectrum consists of 12 levels of the $3s^2 3p^5 3d$ configuration and 4 levels of the $3s 3p^6 3d$ configuration. The energies of these levels are well established experimentally and the present excitation energies agree closely with experimental energies, in the range of 0.35 eV. The energies calculated by Aggarwal *et al.* [13] and Storey *et al.* [11] differ from the experimental energies by up to 1.56 eV except for the $3s^2 3p^5 3d\ ^1P^o_1$ level, where the difference is about 2.1 eV. We note a strong term dependence of the $3d$ orbital for these levels, especially for the ^1P term, which is directly included in the present calculations with the nonorthogonal orbital

TABLE I. Comparison of the present level energies with measured values from NIST and calculated results of Aggarwal *et al.* [13] (A06) and Storey *et al.* [11] (S02). The differences (diff.) between various calculated and experimental values are also listed.

Index	Configuration	LSJ	NIST[a] (eV)	Present (eV)	Diff.	A06[b] (eV)	Diff.	S02[c] (eV)	Diff.
1	$3s^23p^6$	$^1S_0$	0.00	0.00	0.00	0.00	0.00	0.00	0.00
2	$3s^23p^53d$	$^3P^o_0$	50.31	50.31	0.00	50.92	0.61	51.19	0.88
3	$3s^23p^53d$	$^3P^o_1$	50.62	50.64	0.02	51.24	0.62	51.54	0.92
4	$3s^23p^53d$	$^3P^o_2$	51.29	51.32	0.03	51.91	0.62	52.26	0.97
5	$3s^23p^53d$	$^3F^o_4$	52.79	53.05	0.25	53.69	0.90	53.96	1.17
6	$3s^23p^53d$	$^3F^o_3$	53.23	53.46	0.24	54.14	0.91	54.39	1.16
7	$3s^23p^53d$	$^3F^o_2$	53.79	54.00	0.21	54.70	0.92	54.96	1.17
8	$3s^23p^53d$	$^3D^o_3$	56.49	56.80	0.31	57.60	1.11	57.73	1.24
9	$3s^23p^53d$	$^1D^o_2$	56.63	56.86	0.23	57.80	1.17	57.91	1.28
10	$3s^23p^53d$	$^3D^o_1$	57.11	57.35	0.24	58.21	1.10	58.34	1.23
11	$3s^23p^53d$	$^3D^o_2$	57.36	57.59	0.23	58.48	1.12	58.64	1.29
12	$3s^23p^53d$	$^1F^o_3$	57.76	58.06	0.31	58.87	1.11	59.06	1.30
13	$3s^23p^53d$	$^1P^o_1$	72.47	72.78	0.31	74.51	2.04	74.58	2.10
14	$3s3p^63d$	$^3D_1$	90.10	90.26	0.16	91.36	1.26	91.48	1.38
15	$3s3p^63d$	$^3D_2$	90.21	90.37	0.17	91.47	1.26	91.60	1.40
16	$3s3p^63d$	$^3D_3$	90.38	90.56	0.18	91.63	1.26	91.80	1.42
17	$3s3p^63d$	$^1D_2$	92.97	93.32	0.35	94.53	1.56	94.47	1.50
18	$3s^23p^4(^3P)3d^2(^3P)$	$^5S_2$		99.75		101.45		102.16	
19	$3s^23p^4(^3P)3d^2(^3F)$	$^5D_0$		100.40		102.17		102.77	
20	$3s^23p^4(^3P)3d^2(^3F)$	$^5D_1$		100.43		102.20		102.81	
21	$3s^23p^4(^3P)3d^2(^3F)$	$^5D_2$		100.48		102.25		102.87	
22	$3s^23p^4(^3P)3d^2(^3F)$	$^5D_3$		100.55		102.31		102.96	
23	$3s^23p^4(^3P)3d^2(^3F)$	$^5D_4$		100.63		102.39		103.06	
24	$3s^23p^4(^3P)3d^2(^3F)$	$^5F_5$		101.67		103.52		104.15	
25	$3s^23p^4(^3P)3d^2(^3F)$	$^5F_4$		101.74		103.60		104.22	
26	$3s^23p^4(^3P)3d^2(^3F)$	$^5F_3$		101.81		103.69		104.30	
27	$3s^23p^4(^3P)3d^2(^3F)$	$^5F_2$		101.85		103.74		104.34	
28	$3s^23p^4(^3P)3d^2(^3F)$	$^5F_1$		101.88		103.79		104.38	
29	$3s^23p^4(^3P)3d^2(^3F)$	$^5G_5$		103.81		105.87		106.45	
30	$3s^23p^4(^3P)3d^2(^3F)$	$^5G_6$		103.92		105.42		106.01	
31	$3s^23p^4(^3P)3d^2(^3F)$	$^5G_4$		104.08		106.17		106.74	
32	$3s^23p^4(^3P)3d^2(^3F)$	$^5G_3$		104.25		106.37		106.94	
33	$3s^23p^4(^3P)3d^2(^3F)$	$^5G_2$		104.35		106.50		106.86	
34	$3s^23p^4(^3P)3d^2(^1D)$	$^3P_0$		104.37		106.08		106.58	
35	$3s^23p^4(^3P)3d^2(^1D)$	$^3P_1$		104.53		106.25		106.77	
36	$3s^23p^4(^3P)3d^2(^1D)$	$^3P_2$		104.63		106.34		107.05	
37	$3s^23p^4(^3P)3d^2(^3F)$	$^3F_2$		105.33		107.20		107.65	
38	$3s^23p^4(^3P)3d^2(^3F)$	$^3F_3$		105.79		107.68		108.16	
39	$3s^23p^4(^3P)3d^2(^3F)$	$^3F_4$		106.11		108.03		108.55	
40	$3s^23p^4(^3P)3d^2(^1G)$	$^3G_5$		106.22		108.17		108.68	
41	$3s^23p^4(^3P)3d^2(^1G)$	$^3G_4$		106.36		108.32		108.81	
42	$3s^23p^4(^3P)3d^2(^1G)$	$^3G_3$		106.77		108.79		109.29	
43	$3s^23p^4(^3P)3d^2(^1D)$	$^3D_3$		107.84		109.86		111.32	
44	$3s^23p^4(^3P)3d^2(^3F)$	$^1D_2$		107.87		109.76		110.19	
45	$3s^23p^4(^3P)3d^2(^1D)$	$^3F_4$		107.91		110.05		110.50	
46	$3s^23p^4(^3P)3d^2(^1D)$	$^3F_3$		108.58		110.87		110.28	
47	$3s^23p^4(^3P)3d^2(^1D)$	$^3D_2$		108.59		110.81		111.68	
48	$3s^23p^4(^3P)3d^2(^3P)$	$^5D_3$		108.86		110.49		110.90	
49	$3s^23p^4(^3P)3d^2(^3P)$	$^5D_2$		108.87		110.53		111.24	
50	$3s^23p^4(^3P)3d^2(^1D)$	$^3D_1$		108.89		110.95		111.37	
51	$3s^23p^4(^3P)3d^2(^3P)$	$^5D_4$		108.92		110.73		111.16	
52	$3s^23p^4(^3P)3d^2(^3P)$	$^5D_1$		109.02		110.82		111.23	
53	$3s^23p^4(^3P)3d^2(^3P)$	$^5D_0$		109.03		110.90		111.28	
54	$3s^23p^4(^3P)3d^2(^1D)$	$^3F_2$		109.07		111.23		110.94	
55	$3s^23p^4(^1D)3d^2(^3F)$	$^3H_4$		109.22		111.57		111.93	
56	$3s^23p^4(^1D)3d^2(^1D)$	$^1S_0$		109.33		111.12		111.51	
57	$3s^23p^4(^1D)3d^2(^3F)$	$^3H_6$		109.41		111.80		112.23	

TABLE I. (*Continued.*)

Index	Configuration	LSJ	NIST[a] (eV)	Present (eV)	Diff.	A06[b] (eV)	Diff.	S02[c] (eV)	Diff.
58	$3s^23p^4(^1D)3d^2(^3F)$	$^3H_5$		109.42		111.78		112.18	
59	$3s^23p^4(^3P)3d^2(^3P)$	$^5P_3$		109.49		111.44		111.90	
60	$3s^23p^4(^3P)3d^2(^3P)$	$^5P_2$		109.59		111.50		111.95	
61	$3s^23p^4(^3P)3d^2(^3P)$	$^5P_1$		109.64		111.53		111.95	
62	$3s^23p^4(^3P)3d^2(^3P)$	$^3D_2$		110.00		111.99		112.36	
63	$3s^23p^4(^3P)3d^2(^3P)$	$^3D_1$		110.11		112.14		112.53	
64	$3s^23p^4(^1D)3d^2(^1D)$	$^1F_3$		110.30		113.08		112.75	
65	$3s^23p^4(^3P)3d^2(^3P)$	$^3D_3$		110.37		112.35		113.42	
66	$3s^23p^4(^3P)3d^2(^3F)$	$^1G_4$		110.57		112.51		112.88	
67	$3s^23p^4(^1D)3d^2(^3F)$	$^3G_3$		111.05		112.38		112.71	
68	$3s^23p^4(^1D)3d^2(^3P)$	$^3P_2$		111.13		113.11		113.48	
69	$3s^23p^4(^1D)3d^2(^3P)$	$^3P_0$		111.18		113.14		113.51	
70	$3s^23p^4(^1D)3d^2(^3P)$	$^3P_1$		111.21		113.22		113.60	
71	$3s^23p^4(^1D)3d^2(^3F)$	$^3G_4$		111.25		113.20		113.51	
72	$3s^23p^4(^1D)3d^2(^3F)$	$^3G_5$		111.63		113.57		113.91	
73	$3s^23p^4(^1D)3d^2(^1G)$	$^1I_6$		112.11		115.22		115.60	
74	$3s^23p^4(^3P)3d^2(^1G)$	$^3H_6$		112.38		113.53		113.86	
75	$3s^23p^4(^3P)3d^2(^1G)$	$^3H_5$		112.46		114.59		114.94	
76	$3s^23p^4(^3P)3d^2(^1G)$	$^3F_2$		112.70		114.83		115.10	
77	$3s^23p^4(^3P)3d^2(^1G)$	$^3H_4$		112.95		115.10		115.45	
78	$3s^23p^4(^3P)3d^2(^1G)$	$^3F_3$		113.01		115.14		115.43	
79	$3s^23p^4(^1D)3d^2(^1D)$	$^1P_1$		113.35		115.13		115.40	
80	$3s^23p^4(^3P)3d^2(^1G)$	$^3F_4$		113.37		115.50		115.80	
81	$3s^23p^4(^1D)3d^2(^1D)$	$^1G_4$		113.58		116.28		116.65	
82	$3s^23p^4(^3P)3d^2(^3F)$	$^3D_1$		115.81		118.07		118.38	
83	$3s^23p^4(^3P)3d^2(^3F)$	$^3D_2$		115.97		118.30		119.03	
84	$3s^23p^4(^1S)3d^2(^1D)$	$^1D_2$		116.53		118.78		118.57	
85	$3s^23p^4(^3P)3d^2(^3F)$	$^3D_3$		116.81		119.19		119.54	
86	$3s^23p^4(^3P)3d^2(^1S)$	$^3P_2$		117.35		119.31		119.51	
87	$3s^23p^4(^1D)3d^2(^1G)$	$^1H_5$		117.41		119.73		119.94	
88	$3s^23p^54s$	$^3P^o_2$		117.60		120.41		116.82	
89	$3s^23p^4(^1D)3d^2(^3P)$	$^3F_2$		117.63		120.10		120.21	
90	$3s^23p^4(^1D)3d^2(^3P)$	$^3F_3$		117.89		120.38		120.51	
91	$3s^23p^54s$	$^3P^o_1$	117.85	118.20	0.35	121.03	3.18	122.63	4.78
92	$3s^23p^4(^1D)3d^2(^3P)$	$^3F_4$		118.24		120.75		120.89	
93	$3s^23p^4(^3P)3d^2(^1S)$	$^3P_1$		118.39		120.34		120.57	
94	$3s^23p^4(^3P)3d^2(^1S)$	$^3P_0$		118.72		120.68		120.91	
95	$3s^23p^54s$	$^3P^o_0$		119.43		122.33		118.72	
96	$3s^23p^4(^3P)3d^2(^1G)$	$^3G_4$	118.50[d]	119.61	1.11	123.41	4.91	123.88	5.38
97	$3s^23p^4(^3P)3d^2(^1G)$	$^3G_5$	118.57[d]	119.63	1.06	123.47	4.90	123.95	5.38
98	$3s^23p^4(^1D)3d^2(^1G)$	$^3G_3$	118.63[d]	119.69	1.06	123.52	4.89	123.97	5.34
99	$3s^23p^54s$	$^1P^o_1$	119.72	120.03	0.31	122.95	3.23	124.57	4.85

[a]From NIST [10].
[b]From Aggarwal *et al.* [13].
[c]From Storey *et al.* [11].
[d]From Young [19].

technique. We also found very strong core-valence correlations for these levels due to $3p^2$-$3d^2$ promotion in the $3s^23p^33d^3$ and $3s3p^43d^3$ states and these are included in our CI expansions. Aggarwal *et al.* [13] also noted strong interaction between the $3s^23p^33d^3$ and the $3s^23p^43d^2$ configurations.

Next we consider levels of the $3s^23p^43d^2$ configuration in the Fe^{8+} spectrum. We have included 78 levels of the $3s^23p^43d^2$ configuration and 4 levels of the $3s^23p^54s$ configuration in the description of the final residual Fe^{8+} ion. The importance of the $3s^23p^43d^2$ levels has been discussed by Storey *et al.* [11], Aggarwal *et al.* [13], and Liedahl [18] regarding the overall accuracy of energy levels. The calculation by Verma *et al.* [12] did not include levels of the $3s^23p^43d^2$ configuration and this deficiency of their calculation has been discussed in detail by Aggarwal *et al.* [13]. Only a few levels of this configuration are identified from the experimental measurements that can be used for benchmark comparison with theory. Young [19] proposed identification for the multiplet $3s^23p^4(^3P)3d^2(^1G)\ ^3G$ (indexes 96–98 in Table I). Our calculations agree within 1.1 eV with his identifications, while

the calculations of Aggarwal *et al.* [13] and Storey *et al.* [11] differ by about 4.90 and 5.38 eV, respectively. This agreement can be considered reasonable, taking into account the rather strong restriction of CI expansions with a cutoff factor of 0.02 was imposed in order to obtain feasible representation of target states in our subsequent R-matrix photoionization calculations. The present calculation as well as the calculations of Aggarwal *et al.* [13] and Storey *et al.* [11] are *ab initio*, while Verma *et al.* [12] adjusted diagonal elements of the Hamiltonian matrices to bring their calculated energies close to the experimental values. The experimental energies are also available for the $3s^2 3p^5 4s\ ^3P_1$ and $^1P_1$ levels (indexes 91 and 99). The present excitation energies closely agree with experiment, with the same accuracy as for the $3s^2 3p^5 3d$ levels discussed above. The calculations of Aggarwal *et al.* [13] and Storey *et al.* [11] agree to about 3.20 and 4.80 eV, respectively.

The wave functions of the lowest 17 levels are considered to be the most accurate in available calculations, as also noted by Aggarwal *et al.* [13]. The oscillator strengths among these levels should provide the overall accuracy of the final residual ionic states. Comparison of oscillator strengths from two GRASP calculations with 1099 levels of the $3s^2 3p^6$, $3s^2 3p^5 3d$, $3s 3p^6 3d$, $3s^2 3p^4 3d^2$, $3s 3p^5 3d^2$, $3s^2 3p^3 3d^3$, $3s 3p^4 3d^3$, and $3p^6 3d^2$ configurations of the $n = 3$ complex and with 2471 configurations of the $n = 3$ complex, plus additional configurations of the $n = 4$ complex, shows that they normally agree within about 10%, indicating that the $n = 4$ configurations are less important. We have included in Table II the length oscillator strengths and ratios between the length and the velocity values from the present work together with the calculations of Aggarwal *et al.* [13] and Verma *et al.* [12]. There are 23 so-called dipole-allowed and 15 spin-forbidden transitions possible among these 17 levels. The oscillator strengths for the spin-forbidden transitions are usually lower than the dipole-allowed transitions, as these transitions are induced by the spin-orbit interaction due to mixing of different LS symmetries with the same J and π quantum numbers. The dipole-allowed $3s^2 3p^6\ ^1S_0$–$3s^2 3p^5 3d\ ^1P_1^o$ transition is the strongest transition and our length and velocity values agree to 5%. Our length value agrees within 3% with Aggarwal *et al.* [13] and Verma *et al.* [12].

Next we discuss transitions with oscillator strengths $\geqslant 0.01$ where the agreement between the present length and velocity formulations varies from 19% to 35%, with an average difference of about 25%. The results of Aggarwal *et al.* [13] exhibit a similar agreement between the length and the velocity forms, with an overall agreement of about 20% for these transitions. Though the wave functions and CI expansions of Verma *et al.* [12] are deficient as discussed by Aggarwal *et al.* [13], their length and velocity results show on average a 20% difference. The oscillator strengths of Aggarwal *et al.* [13] for this group of transitions are higher than our results by 20%–25%. The calculation of Aggarwal *et al.* [13] is considered to be the most extensive and our results for the 2-14, 3-14, 3-15, 4-15, 4-16, and 11-15 transitions are within 20% and differ by about 25% for the remaining transitions. For the weaker transitions with oscillator strengths less than 0.01 all calculations show varied degrees of differences between the two forms: on average, about 50%. The agreement between the length and the velocity forms is, to some extent, an indicator of the accuracy of wave functions and the convergence of CI expansions, but it is not necessarily a sufficient condition as demonstrated by several calculations in the past including the work byAggarwal *et al.* [13]. It is possible that the agreement between the length and the velocity values may occur even with very simple wave functions. It may be noted that there is a strong interaction between many levels of Fe^{8+} because of the proximity of the levels as well as the strong interaction between Rydberg series and perturbers. The strong mixing between the levels is sensitive to the choice of wave functions and CI expansions. The cancellations in dipole matrix elements of the main configurations of the initial

TABLE II. Comparison of oscillator strengths, as the length formulation and the ratio of length and velocity values, for transitions between the first 17 levels of Fe^{8+} from the present calculation, the GRASP calculation by Aggarwal *et al.* [13], and the CIV3 calculation by Verma *et al.* [12]. Numbers in brackets indicate the power of 10.

	Present		GRASP		CIV3	
Transition	f_L	Ratio	f_L	Ratio	f_L	Ratio
1-3	3.35[−4]	0.81	3.70[−4]	0.95	3.38[−4]	0.47
1-10	5.32[−3]	0.77	5.53[−3]	0.94	5.56[−3]	0.61
1-13	3.07[+0]	1.05	3.15[+0]	0.96	2.98[+0]	0.98
2-14	5.73[−2]	1.33	6.95[−2]	1.20	5.29[−2]	1.10
3-14	1.75[−2]	1.35	2.14[−2]	1.20	1.62[−2]	1.10
3-15	4.04[−2]	1.26	4.87[−2]	1.20	3.75[−2]	1.10
3-17	1.44[−4]	1.43	1.55[−4]	1.10	1.77[−6]	12.0
4-14	1.11[−3]	1.40	1.37[−3]	1.20	1.03[−3]	1.10
4-15	1.22[−2]	1.31	1.49[−2]	1.20	1.14[−2]	1.10
4-16	4.61[−2]	1.19	5.51[−2]	1.20	4.27[−2]	1.10
4-17	2.14[−4]	1.52	3.56[−4]	0.79	1.44[−4]	0.84
5-16	2.98[−2]	1.33	4.07[−2]	0.68	2.37[−2]	0.61
6-15	2.79[−2]	1.28	3.79[−2]	0.69	2.21[−2]	0.61
6-16	1.06[−3]	1.02	1.48[−3]	0.46	6.95[−4]	0.39
6 17	2.21[−4]	1.52	4.03[−4]	1.00	7.11[−4]	0.97
7-14	2.65[−2]	1.22	3.59[−2]	0.69	2.12[−2]	0.59
7-15	1.63[−3]	0.98	2.32[−3]	0.49	1.14[−3]	0.41
7-16	4.93[−6]	1.56	8.54[−6]	4.10	1.92[−5]	21.0
7-17	7.75[−4]	1.52	1.12[−3]	0.62	7.12[−4]	0.68
8-15	1.55[−3]	1.40	2.20[−3]	1.10	1.66[−3]	0.86
8-16	1.88[−2]	1.33	2.47[−2]	1.00	1.48[−2]	0.84
8-17	5.80[−3]	1.39	8.07[−3]	0.88	5.96[−3]	0.77
9-15	8.26[−3]	1.20	1.30[−2]	0.95	6.29[−3]	0.71
9-16	1.04[−3]	1.30	2.13[−3]	1.00	8.60[−4]	0.79
9-17	1.24[−2]	1.29	1.68[−2]	0.61	9.93[−3]	0.55
10-14	1.84[−2]	1.27	2.49[−2]	1.00	1.53[−2]	0.77
10-15	9.80[−3]	1.16	1.27[−2]	1.10	8.57[−3]	0.77
10-17	1.48[−5]	1.07	4.43[−5]	0.64	9.07[−6]	1.00
11-14	1.92[−3]	1.31	2.65[−3]	1.10	1.62[−3]	0.83
11-15	1.13[−2]	1.27	1.33[−2]	1.00	9.69[−3]	0.76
11-16	7.62[−3]	1.07	8.83[−3]	1.10	6.94[−3]	0.76
11-17	5.49[−3]	1.24	1.02[−2]	0.64	3.56[−3]	0.52
12-15	1.78[−5]	0.64	1.97[−6]	28.0	1.58[−5]	0.06
12-16	8.59[−3]	1.12	1.20[−2]	0.98	8.28[−3]	0.70
12-17	1.40[−2]	1.20	1.77[−2]	0.85	1.11[−2]	0.70
13-14	1.58[−5]	0.65	1.33[−5]	0.94	9.25[−6]	0.13
13-15	1.23[−4]	0.65	1.01[−4]	0.71	2.41[−5]	0.23
13-17	6.54[−4]	2.15	7.05[−3]	0.30	1.64[−3]	0.15

and final states of a transition generally give rise to weaker transitions. The correlation corrections play a particularly important role for weaker transitions. The overall agreement of the present oscillator strengths with the GRASP results for transition between all target states of Fe^{8+} is within 20% for 38% of transitions and within 50% for the remaining 62% of transitions. These values can be considered as an overall estimation of the accuracy of available radiative data for Fe^{8+}.

B. Photoionization calculations

Photoionization calculations have been performed with the B-spline R-matrix (BSR) code [20]. This code employs the B-spline Breit-Pauli R-matrix method, which was described in detail in our previous electron-impact calculations for Fe^{7+} [21] and Fe^{6+} [22]. The method uses the B splines as a universal basis to represent the scattering orbitals in the inner region of $r \leqslant a$. Hence, the R-matrix expansion in this region takes the form

$$\begin{aligned}\Psi_k(x_1,\ldots,x_{N+1}) &= \mathcal{A}\sum_{ij}\bar{\Phi}_i(x_1,\ldots,x_N;\hat{\mathbf{r}}_{N+1}\sigma_{N+1})\,r_{N+1}^{-1}\,B_j(r_{N+1})\,a_{ijk} \\ &+ \sum_i \chi_i(x_1,\ldots,x_{N+1})\,b_{ik}. \end{aligned} \quad (2)$$

Here the $\bar{\Phi}_i$ denote the channel functions constructed from the N-electron target states, while the splines $B_j(r)$ represent the continuum orbitals. The χ_i are additional $(N+1)$-electron bound states. In standard R-matrix calculations [23], these are included to ensure completeness of the total trial wave function and to compensate for orthogonality constraints imposed on the continuum orbitals. The use of nonorthogonal one-electron radial functions in the BSR method, on the other hand, allows us to completely avoid these configurations for compensating orthogonality restrictions. This procedure has practical advantages in reducing pseudoresonance structure in the scattering solutions (as an example, see the discussion in Ref. [24]).

The continuum orbitals in the internal region with radius $a = 15a_0$ were represented by 78 B splines of order 8, with the maximum interval in this grid of $0.65a_0$. This is sufficient for a good representation of the scattering electron wave functions for energies up to 200 eV. The present BSR-99 collision model contained up to 494 scattering channels. In the R-matrix theory, the photoionization cross sections can be defined through the dipole matrix between the initial state Ψ_0 and the R-matrix basis states Ψ_k provided that all radial orbitals of the initial state are well confined in the inner region. The total photoionization cross section for a given photon energy ω is

$$\sigma(\omega) = \frac{8}{3}\pi^2 a_0^2 \alpha\omega^{\pm 1}\frac{1}{(2J_0+1)}\sum_j |(\Psi_j^-||D||\Psi_0)|^2, \quad (3)$$

where D is a general dipole operator, which can be either the length or the velocity operator, and the signs $(+1)$ and (-1) correspond to the length and velocity forms. The index j goes over different open channels, and other quantities have their usual meaning. Expanding Ψ_j^- in terms of the R-matrix states, we find that

$$(\Psi_j^-||D||\Psi_0) = \frac{1}{a}\sum_k \frac{(\Psi_k||D||\Psi_0)}{E_k - E_0 - \omega}\mathbf{P}_k^T\mathbf{R}^{-1}\mathbf{F}_j^-(a), \quad (4)$$

where $\mathbf{P}_k$ is the vector of the surface amplitudes for R-matrix solutions Ψ_k, and $\mathbf{F}^-$ is constructed from the solutions in the outer region such that it satisfies the boundary condition

$$\mathbf{F}^- \to (\pi k)^{-1/2}(\sin\theta + \cos\theta\mathbf{K})(1 + i\mathbf{K})^{-1}, \quad (5)$$

corresponding to a Coulomb modified plane wave plus an ingoing spherical wave. The ASYPCK program [25] has been employed to find the asymptotic solutions. The wave functions Ψ_0 in Eq. (4) were taken from our previous calculations of electron scattering on Fe^{7+} [21]. They were obtained in intensive MCHF calculations, and the ground-state ionization potential of 151.05 eV is in excellent agreement with the experimental value of 151.06 eV. Note that it is an independent calculation, with full inclusion of the possible relaxation effects. The ionization threshold for the Fe^{7+} ground state is 151.146 eV from the CI calculation of Sossah *et al.* [7], which is in good agreement with our calculation and experiment.

III. RESULTS

We have attempted to improve theoretical calculations by using an accurate representation of the electron correlation effects for both the Fe^{7+} initial bound levels and the final Fe^{8+} ion plus photoelectron levels in a consistent and balanced manner with nonorthogonal BSR basis functions. The theoretical photoionization calculations have also been improved by including a larger set of residual Fe^{8+} ion levels, generated within the framework of a combination of MCHF and the B-spline box-based multichannel methods as described in Sec. II. The earlier calculation by Sossah *et al.* [7] included 17 levels, whereas the present work includes 99 levels. The photoionization of a $3p$ or $3s$ electron from the Fe^{7+} initial ground configuration $3s^23p^63d\ ^2D_{3/2,5/2}$ levels give rise to Fe^{8+} $3s^23p^53d$ and $3s3p^63d$ levels (levels 1–17 in Table I). The Fe^{8+} levels of the $3s^23p^43d^2$ and $3s3p^54s$ configurations (levels 18–99 in Table I) account for the photoionization process where a photoelectron is ejected and a second electron is promoted to an excited level. The $3s^23p^43d^2$ levels are also important for photoionization from metastable states discussed below.

The ground initial level of Fe^{7+} is $3s^23p^63d\ ^2D_{3/2}$ and the $^2D_{5/2}$ level of the ground configuration is a metastable level at 0.228 eV. The $3s^23p^53d^2$ and $3s^23p^64s$ configurations also provide many metastable or quasimetastable levels. The identification of possible metastable levels is very important for interpretation of measured photoionization cross sections because the beam of ions may contain a significant population of metastable levels. In particular, metastable states are expected to be present in the primary ion beam of recent measurements by Gharaibeh *et al.* [6] if their lifetimes are comparable to or greater than their flight time in the apparatus ($\sim 10^{-5}$ s). Thus the primary Fe^{7+} ion beam consists of an unknown admixture of ions in the ground level and in metastable levels, and the measured photoions can originate from any of these levels. It may enhance the measured photoion yield spectrum, but it also complicates comparison with

TABLE III. Metastable states of Fe^{7+}. Numbers in brackets indicate the power of 10.

Index	Configuration	LSJ	E (eV)	Lifetime (s)
1	$3p^6 3d$	$^2D_{3/2}$	0.00	
2	$3p^6 3d$	$^2D_{5/2}$	0.23	1.10[+01]
8	$3p^5 3d^2(^3F)$	$^4G_{11/2}$	51.36	5.90[+02]
9	$3p^5 3d^2(^3F)$	$^4G_{9/2}$	51.55	1.86[+00]
11	$3p^5 3d^2(^3F)$	$^4G_{7/2}$	51.77	1.02[−04]
17	$3p^5 3d^2(^3F)$	$^4F_{9/2}$	53.30	4.36[−02]
26	$3p^5 3d^2(^1G)$	$^2H_{11/2}$	55.75	9.79[−01]
28	$3p^5 3d^2(^3F)$	$^2G_{9/2}$	56.49	1.54[−02]
29	$3p^5 3d^2(^1G)$	$^2H_{9/2}$	56.91	2.52[−02]
39	$3p^5 3d^2(^1G)$	$^2G_{9/2}$	60.73	9.05[−03]

theoretical calculations. Systematic calculations of lifetimes for Fe^{7+} levels were provided in our previous publication [21], and levels with a lifetime greater than 10^{-5} are listed in Table III. Any of these states may contribute to the photoion yield in the measurements by Gharaibeh *et al.* [6].

The photoionization process can occur through direct photoionization, where the photon knocks out an electron from the Fe^{7+} ion leaving a residual Fe^{8+} ion. Photoionization can also occur through indirect process where the incident photon excites the ion to autoionizing resonance states that eventually decay by emitting an electron. The former process gives rise to background nonresonant cross sections and later to series of Rydberg resonances. The present work and the previous TOPbase and BPRM calculations include both processes and the interference between them. The direct nonresonant photoionization cross sections and the positions and numbers of resonances from the TOPbase calculation show substantial discrepancies with the measured results. We begin our discussion with the photoionization cross sections from the ground $3s^2 3p^6 3d\ ^2D_{3/2}$ level. Our calculation has been carried out across the autoionizing Rydberg series of resonances converging to various residual ionic levels of Fe^{8+}. In the present work we have focused on the photon energy range from ionization threshold to 172 eV, where measured cross sections are available. We have calculated partial and total photoionization cross sections for the $3p$ and $3s$ subshells of the ground level in both length and velocity formulations. The final $^2P^o_{1/2,3/2}$, $^2D^o_{3/2,5/2}$, and $^2F^o_{5/2}$ levels, that is, $J = 1/2$, $3/2$, and $5/2$ levels, are allowed for photionization from the ground $3s^2 3p^6 3d\ ^2D^o_{3/2}$ level. The total photoionization cross section is determined by adding partial cross sections for final levels with $J = 1/2$, $3/2$, and $5/2$, which in turn are obtained by combining the channel cross sections. The partial cross sections together with the total photoionzation cross sections from the initial ground $3s^2 3p^6 3d\ ^2D_{3/2}$ level are displayed in Fig. 1 from the $3p$ ionization threshold to 172 eV. The lower three panels show the partial cross sections for $J = 1/2$, $3/3$, and $5/2$, respectively, and the top panel shows the total photoionization cross section. The length and velocity results are shown by solid black and dashed (red) curves, respectively. There is normally an excellent agreement between the length and the velocity forms, and this provides some indication that our theoretical results are likely to be accurate. The excitation

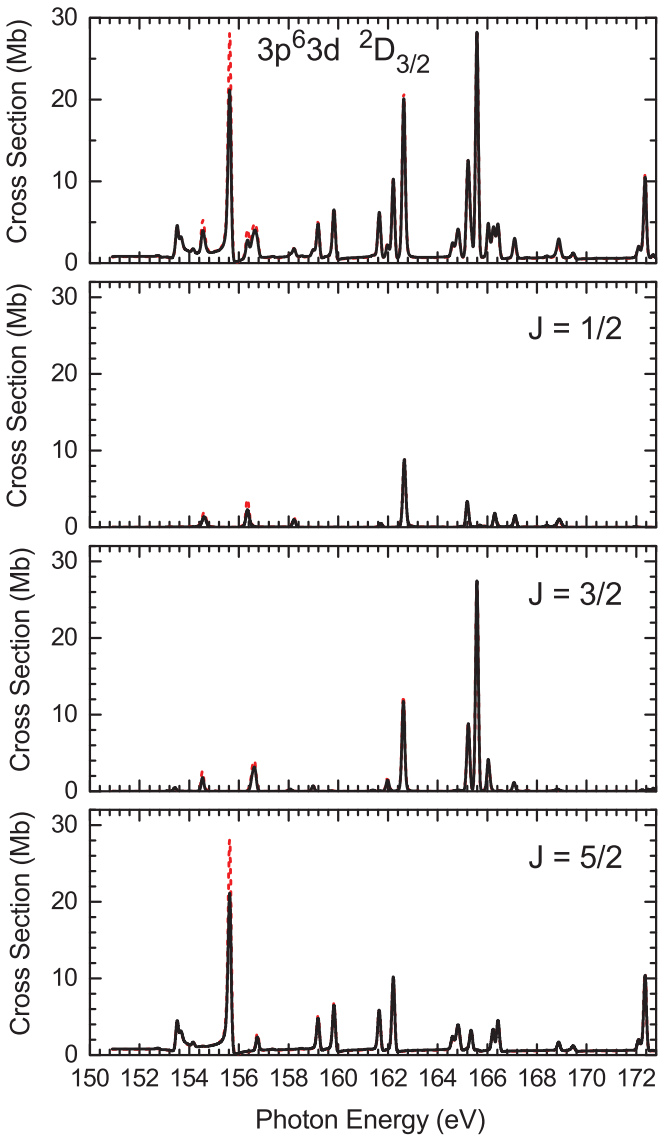

FIG. 1. (Color online) Present B-spline Breit-Pauli R-matrix (BSR) cross sections for photoionization of Fe^{7+} from the ground $3s^2 3p^6 3d\ ^2D_{3/2}$ level (top panel), in both length and velocity formulations. Partial photoionization cross sections, in both length and velocity forms, are shown for $J = 1/2$, $3/2$, and $5/2$ in the lower three panels. Solid black curve, length value; dashed (red) curve, velocity value. Cross sections are convoluted with a Gaussian of FWHM = 0.126 eV to simulate the experimental energy resolution.

of $3p$ electrons into Rydberg orbitals produces $3s^2 3p^5 3dnl$ and $3s^2 3p^5 3dns$ series of Rydberg resonances converging to various Fe^{8+} ionization thresholds. The photoionization cross section shows significant resonance structure, with a dominant contribution from the $J = 5/2$ partial cross section and a weak contribution from the $J = 1/2$ partial cross section. The $J = 5/2$ partial cross section also mostly contributes to the background nonresonant cross section away from resonances. The photoionization cross sections have been calculated at the very fine energy grid of 10^{-4} eV to resolve sharp resonances. The cross sections are then convoluted with a Gaussian of FWHM = 0.126 eV to simulate the experimental energy

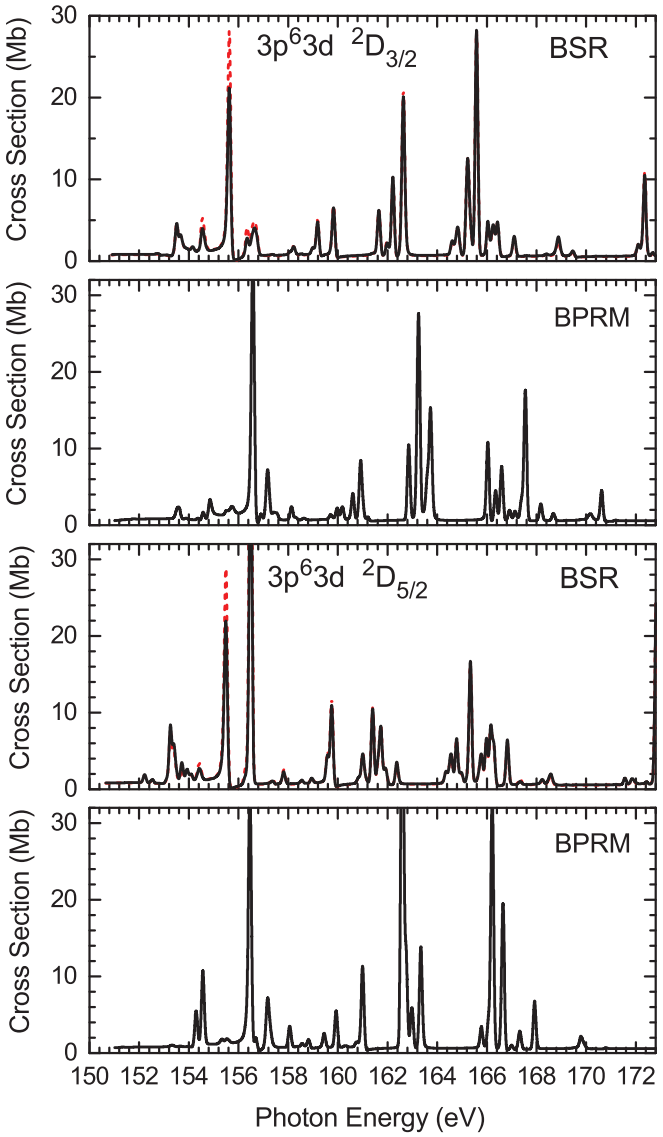

FIG. 2. (Color online) Comparison of the present B-spline Breit-Pauli R-matrix (BSR) cross sections, in length (solid black curve) and velocity [dashed (red) curve] forms, for photoionization of Fe^{7+} with the Breit-Pauli R-matrix (BPRM) calculations [7]. Theoretical cross sections are given for the ground $3s^2 3p^6 3d\ ^2D_{3/2}$ and metastable $^2D_{5/2}$ initial states and convoluted with a Gaussian of FWHM = 0.126 eV to simulate the experimental energy resolution.

resolution. The resonances at around 153.6 and 155.5 eV in the total cross section are contributed by the $J = 5/2$ final levels, while the narrow resonance around 165.6 eV arises from the $J = 3/2$ final levels. The other major resonance in the spectrum around 162.5 eV arises due to the combined $J = 1/2$ and 3/2 final levels, and the resonance around 162.2 eV is again due to the $J = 5/2$ final levels. The resonances around 155.5, 162.5, and 165.6 eV have a magnitude larger than 20 Mb.

We compare the present total photoionization cross sections from the $^2D_{3/2,5/2}$ levels with the BPRM results [7] in Fig. 2. The results are plotted in the photon energy range from 150 to 172 eV. Both theoretical cross sections were convoluted with a Gaussian of FWHM = 0.126 eV to simulate the experimental energy resolution. The present results are labeled BSR, and the calculations by Sossah *et al.* [7] BPRM, in Fig. 2. Our BSR results are shown in both length and velocity formulations by solid black and dashed (red) curves, respectively. There is excellent agreement between the length and the velocity results, and the two curves are almost superimposed except for the peak values of the first few resonances, where the velocity value is larger than the length value. There is generally a good agreement between the two calculations except for some shift in the position and magnitude of resonances. The discrepancies between the two calculations are caused by the differences in wave functions used in the descriptions of the initial Fe^{7+} bound levels and final continuum levels and the residual ionic Fe^{8+} ionization thresholds. We have tried to represent both the initial and the final levels by accounting for electron correlation effects consistently. The direct nonresonant photoionization cross sections are quite small and there is relatively little interaction between resonant and nonresonant contributions. Owing to several interacting series of Rydberg resonances, the photoionization cross sections exhibit a complex resonance structure. The present cross sections statistically weighted over fine-structure levels of the ground configuration terms are presented in the Fig. 3 together with the TOBbase data and the calculation by Sossah *et al.* [7] obtained with the LS R-matrix approach. The top panel in Fig. 3 shows the measured cross sections [6] and the other three panels display the BSR, BPRM, and TOPbase theoretical results. The cross sections contain many resonances due to the $3s^2 3p^5 3dnd$ and $3s^2 3p^5 3dns$ Rydberg series. The present BSR calculations and the R-matrix results of Sossah *et al.* [7] provide a richer resonance structure than the TOPbase data. The theoretical positions and numbers of resonances in the present calculation seem to have improved agreements with measurements relative to BPRM calculations at least in terms of the richness of resonance structures. However, the strengths of resonances differ considerably from the measurements. Integrating the apparent experimental cross section over the energy range from 150 to 172 eV gives an effective oscillator strength of 1.31 ± 0.39. This should be compared to a theoretical value of 0.31 for photoionization from the $^2D_{3/2}$ initial state and a value of 0.29 for photoionization from the $^2D_{5/2}$ initial state. It is evident that any share population of the ground-configuration states will provide cross sections with approximately the same strength but different resonance structures. The background cross sections from the three calculations agree very closely. The effective oscillator strength for the TOPbase cross sections in the given energy region is 0.25 and also closely agrees with the present data.

The above comparison shows that photoionization from the ground-configuration levels cannot explain the difference from experimental absolute normalization. Another possible reason could be the considerable population of other higher excited metastable levels. To check this possibility, we calculated the photoionization cross sections from the $^4G_{9/2}$ and $^4G_{11/2}$ levels, which, according to Table III, are the longest-living and lowest metastable states from the $3p^5 3d^2$ configuration. The results are presented in Fig. 4. These cross sections have slightly larger background cross-section values but show a less intense resonance structure. The effective oscillator strengths for these states over the energy range from 150 to 172 eV

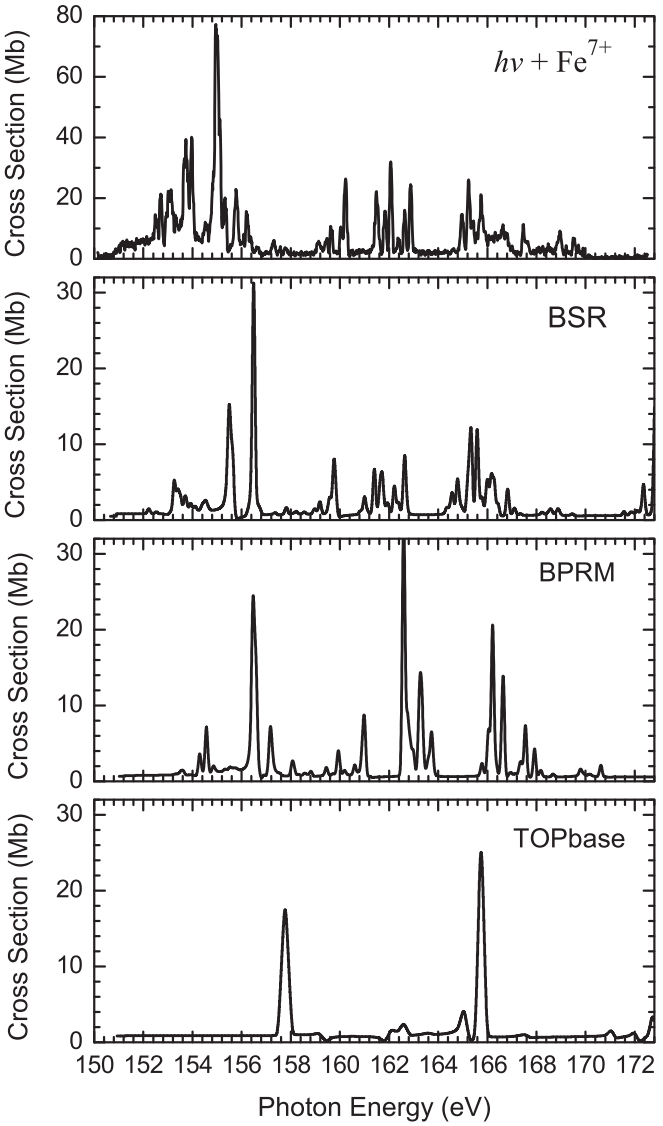

FIG. 3. Comparison of the measured absolute cross section [6] (top panel) for photoionization of Fe^{7+} with the present calculations (BSR), BPRM calculations [7], and TOPbase theoretical data. Theoretical cross sections are given for the $3s^2 3p^6 3d\ ^2D$ initial state and convoluted with a Gaussian of FWHM = 0.126 eV to simulate the experimental energy resolution.

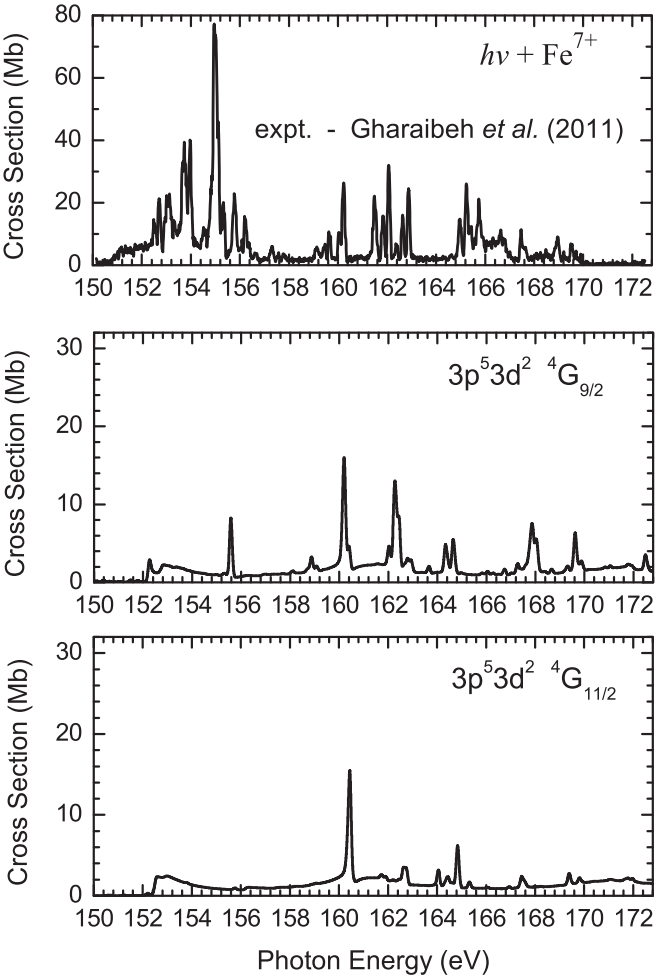

FIG. 4. Comparison of the measured absolute cross section [6] (top panel) for photoionization of Fe^{7+} with the present calculations for the metastable states. Theoretical cross sections are given for the metastable $3s^2 3p^5 3d^2\ ^4G_{9/2}$ and $^4G_{11/2}$ initial states and convoluted with a Gaussian of FWHM = 0.126 eV to simulate the experimental energy resolution.

are 0.28 and 0.27, respectively. These values are very close to the results for excitation from the ground level. Therefore, the population of these levels in the initial electron beam would not lead to enhancement of the photoion yield. Note that we may expect approximately the same absolute values for the cross sections for photoionization from other terms of the $3p^5 3d^2$ configuration because they all have a close configuration composition. We included $3s$, $3p$, and $3d$ ionization channels in our target-state expansions. The $3s$ ionization was found to be very weak relative to the $3p$ and $3d$ ionization.

IV. SUMMARY

In this article we have presented new detailed calculations of the photoionization of Fe^{7+} from both the ground state and the metastable levels. Calculation of the structure and dynamics of $3d$ open subshell ions is a challenging task because of the importance of electron correlation and interchannel coupling effects. The present calculations were motivated partly by the considerable diversity of the existing theoretical and experimental data. Calculations were carried out using the BSR method [20] in the semirelativistic Breit-Pauli approximation. The MCHF method in connection with B-spline expansions was employed for an accurate representation of the initial and final levels of Fe^{7+} as well as the residual final target wave functions of Fe^{8+}. The close-coupling expansion for the photoionization continuum includes 99 fine-structure levels of Fe^{8+}, which completely cover the energy region under investigation, from the threshold to 172 eV. Our photoionization cross sections in length and velocity forms show excellent agreement.

The present background photoionization cross sections agree well with the TOPbase data and with the more recent Breit-Pauli R-matrix calculations [7] but show large discrepancies with the experiment. The resonance structure in

our calculation shows good agreement with the Breit-Pauli R-matrix calculations [7] and, to a lesser extent, with the TOPbase data. There is a qualitative agreement between the present resonance structure and experiment. The resonance structure in the cross sections from the measurement is more intense and shows significant differences in the position and magnitude of resonances with respect to theoretical results. The experimental effective oscillator strengths over the energy range 150–172 eV considerably exceed the calculated values, by up to a factor of 4. The cross sections for photoionization of metastable states were found to have approximately the same magnitude as the cross sections for photoionization of the ground state, thereby the presence of metastable states in the ion beam cannot be the reason for the strong enhancement of the measured cross sections. It may also be noted that the measurement was carried out on resonances because of the low values of ion beam current and nonresonant cross section. The uncertainties in the absolute cross-section scale in the experiment is estimated to be $\pm 30\%$. The high local concentration of oscillator strengths around 153 eV in the measurements compared to calculated results is perhaps also an indication of normalization error. Based on these findings we suggest that the experimental normalization could be in error, and additional measurements are desirable to resolve the large discrepancies between theory and experiment.

ACKNOWLEDGMENTS

We thank R. A. Phaneuf and A. M. Sossah for supplying photoionization data in numerical form. This work was supported by NASA under Grant No. NNX11AB62G from the Solar and Heliophysics program and the U.S. National Science Foundation under Grant No. PHY-0244470.

[1] N. R. Badnell, M. A. Bautista, K. Butler, F. Delahaye, C. Mendoza, P. Palmeri, C. J. Zeippen, and M. J. Seaton, Month. Not. R. Astron. Soc. **360**, 458 (2005).
[2] C. Mendoza, Comput. Phys. Commun. **121-122**, 74 (1999).
[3] H. Kjeldsen, B. Kristensen, F. Folkmann, and T. Andersen, J. Phys. B **35**, 3655 (2002).
[4] J. M. Bizau, C. Blancard, D. Cubaynes, F. Folkmann, D. Kilbane, G. Faussurier, H. Luna, J. L. Lemaire, J. Blieck, and F. J. Wuilleumier, Phys. Rev. A **73**, 020707 (2006).
[5] N. El Hassan, J. M. Bizau, C. Blancard, P. Cossé, D. Cubaynes, G. Faussurier, and F. Folkmann, Phys. Rev. A **79**, 033415 (2009).
[6] M. F. Gharaibeh *et al.*, Phys. Rev. A **83**, 043412 (2011).
[7] A. M. Sossah, H.-L. Zhou, and S. T. Manson, Phys. Rev. A **82**, 043416 (2010).
[8] O. Zatsarinny and C. Froese Fischer, Comput. Phys. Commun. **180**, 2041 (2009).
[9] C. Froese Fischer, Comput. Phys. Commun. **176**, 559 (2007).
[10] http://physics.nist.gov/cgi-bin/AtData
[11] P. J. Storey, C. J. Zeippen, and M. Le Dourneuf, Astron. Astrophys. **394**, 753 (2002).
[12] N. Verma, A. K. S. Jha, and M. Mohan, Astrophys. J (Suppl.) **164**, 297 (2006).
[13] K. M. Aggarwal, F. P. Keenan, T. Kato, and I. Murakamia, Astron. Astrophys. **460**, 331 (2006).
[14] W. Eissner, M. Jones, and H. Nussbaumer, Comput. Phys. Commun. **8**, 270 (1974).
[15] A. Hibbert, Comput. Phys. Commun. **9**, 141 (1975).
[16] K. G. Dyall, I. P. Grant, C. T. Johnson, F. A. Parpia, and E. P. Plummer, Comput. Phys. Commun. **55**, 425 (1989).
[17] M. F. Gu, Astrophys. J. **582**, 1241 (2003).
[18] D. A. Liedahl, Atomic data needs for x-ray astronomy. Available at: http://heasarc.gsfc.nasa.gov/docs/heasarc/atomic/
[19] P. R. Young, Astrophys. J. **691**, L77 (2009).
[20] O. Zatsarinny, Comput. Phys. Commun. **174**, 273 (2006).
[21] S. Tayal and O. Zatsarinny, Astrophys. J. **743**, 206 (2011).
[22] S. Tayal and O. Zatsarinny, Astrophys. J. **788**, 24 (2014).
[23] P. G. Burke, *R-Matrix Theory of Atomic Collisions* (Springer-Verlag, Berlin, 2011).
[24] S. S. Tayal and O. Zatsarinny, Phys. Rev. A **78**, 012713 (2008).
[25] M. A. Crees, Comput. Phys. Commun. **19**, 103 (1980).